Hydrographic section along 55°E in the Indian and Southern oceans

Katsuro Katsumata[1], Shigeru Aoki[2], Kay I. Ohshima[2], and Michiyo Yamamoto-Kawai[3]

[1]Graduate School of Science, University of Tokyo
[2]Institute of Low Temperature Science, Hokkaido University
[3]Department of Ocean Sciences, Tokyo University of Marine Science and Technology

Correspondence: Katsuro Katsumata (katsumata@eps.s.u-tokyo.ac.jp)

Abstract. A hydrographic section along 55°E, south of 30°S, was visited from December 2019 to January 2020 as the first occupation under the Global Ocean Ship-based Hydrographic Investigation Program. The water column was measured from the sea surface to 10 dbar above the bottom with eddy-resolving station spacings and the state-of-the-art accuracy. The upper profile was characterised by a conspicuous front between 42.5° and 43°S and a cold-core eddy at 39°S. The front was identified as the confluence of Subtropical and Subantarctic fronts. The Agulhas Return Current front was found at 41.6°S. When combined with the section north of 30°S observed in 2018, another subsurface front was found in dissolved oxygen around 28°S at depths of 1500 to 3000 dbar. In the eastern Weddell-Enderby Abyssal Plain, no obvious large scale flow was observed at depths greater than 3000 dbar. We used transient tracers to estimate isopycnal diffusivity there to be 72 ± 16 $\mathrm{m^2 s^{-1}}$. Antarctic Bottom Water in the basin consisted of water masses originating from the Cape Darnley region ($0-35\%$) and Weddell Sea Deep Water ($5-75\%$), diluted by Lower Circumpolar Deep Water above. These snapshot observations not only confirm hydrographic features reported earlier in the Madagascar and Crozet Basins, but also describe the diffusive nature of the deep to bottom circulation in the Weddell-Enderby Abyssal Plain.

1 Introduction

Antarctic Bottom Water (AABW) produced around Antarctica spreads equatorward mainly along the western boundaries of the ocean basins. For this reason, hydrographic sections revealing the deep water masses along 50°E or 60°E in the Indian Ocean have often been discussed in the context of global-scale circulation (e.g. Johnson, 2008; Mantyla and Reid, 1983). Nevertheless, synoptic hydrographic observations of these sections (Warren, 1978; Park et al., 1993) are rare mainly because of logistical difficulties. The GO-SHIP (Global Ocean Ship-based Hydrographic Investigations Program) section I07S is one of these sections and occupied for the first time in the austral summer of 2019/20. It extends the existing section (I07N; equatorward of 30°S) to Cape Ann, the northernmost point in the East Antarctica (Fig. 1).

The section follows the approximate flow path of AABW, and also crosses the Antarctic Circumpolar Current (ACC). When the ACC, which manifests as a bundle of fronts, flows between or over topographic features, mesoscale eddies are produced. The section crosses these fronts and eddies (Fig. 1). These fronts as well as water masses at shallow and intermediate depths have been extensively studied in a series of cruises by Y.-H.Park (Park et al., 1991, 1993; Park and Gambéroni, 1997; Park et al., 1998) and by later cruises (e.g. Meijers et al., 2010; Williams et al., 2010; Jullion et al., 2014; Ryan et al., 2016). In contrast, the
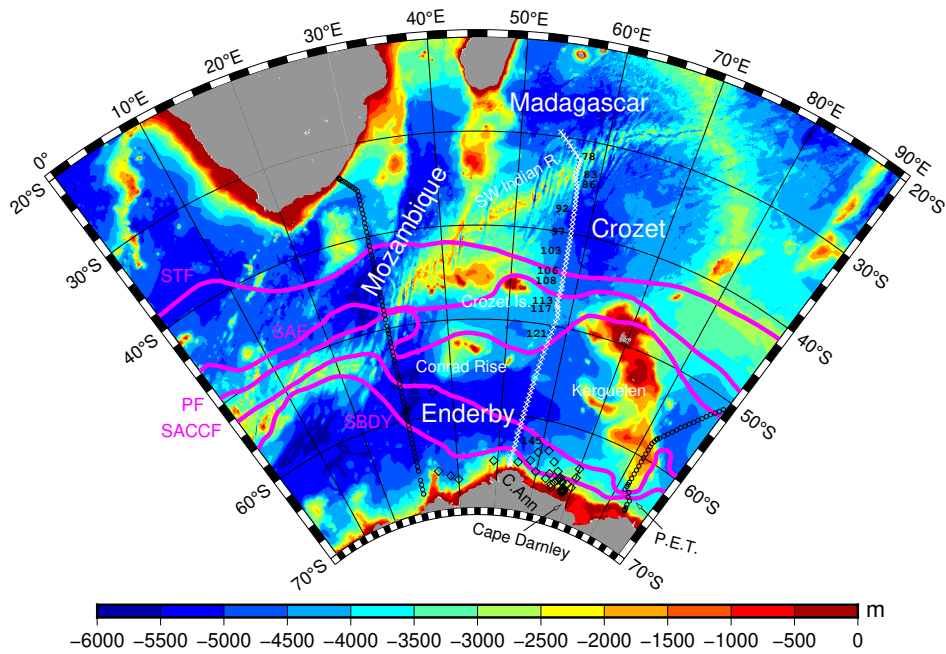
Figure 1. ETOPO5 bathymetry (colour scale) with basin names and topographic features, C.Ann (Cape Ann), and P.E.T. (Princess Elizabeth Trough). The white crosses between 50°E and 60°E indicate the I07S section; the black circles at 30°E indicate the I06S section; and those between 80°E and 90°E indicate the I08S section (stations occupied in 2007). Selected stations along the I07S section are labelled. The southernmost station is 153. The diamonds near the coast of Antarctica are R/V *Hakuho* (KH) cruise stations. The magenta lines show the climatological positions of the five major fronts as defined by Orsi et al. (1995); Subtropical Front (STF), Subantarctic Front (SAF), Polar Front (PF), Southern Antarctic Circumpolar Current Front (SACCF), and Southern Boundary (SBDY).

deep circulation within the Weddell-Enderby Abyssal Plain has received limited attention. In this paper, for convenience, we call the eastern part of the Abyssal Plain as the Enderby Basin. The northern limb of the gyral circulation within the Enderby Basin is an eastward flow along the southern flank of the Southwest Indian Ridge; Gordon and Huber (1984) called this flow as the Weddell Cold Regime because the water mass is mixed with cold winter water produced along the coastal shelves of the Weddell Sea. This cold water mixes with relatively warm water carried by the ACC to form the Weddell Warm Regime, which flows westward as the southern limb of the Weddell Gyre. The eastern boundary of the Weddell Gyre has not been clearly defined by observation data. Direct measurement of velocity by a lowered Acoustic Doppler Current Profiler (Meijers et al., 2010) suggests that the boundary is close to 40°E. Jullion et al. (2014) used a box inverse model to estimate transports across the I06S section (30°E). They found the zonal transport in deep to bottom layers to be mostly eastward along the southern flank of the Southwestern Indian Ridge, but it includes both eastward and westward components in the interior of the Enderby Basin. Further south near the coast, the transport is dominated by a westward flow along the Antarctic Slope Front. It is not clear how these structures extend eastward to the I07S section at 55°E. Here, we examine the deep circulation in the Enderby Basin as revealed by hydrographic data collected along the section where it passes through the basin.

As the subtropical frontal jet of the ACC negotiates the Southwest Indian Ridge around 45°E, 40°S, vigorous eddies are produced to leeward over the Crozet Basin (Fig. 2). At 1000 dbar depth, eddy activity is also seen at around 30°E, 50°S and its effects extend to the Enderby Basin to leeward. The difference between the surface and 1000 dbar might be attributable to the choice of contour values, and to weaker stratification over the Enderby Basin, or both. Our analysis shows that, because of these eddies, the deep circulation in the Enderby Basin is diffusive (see Section 4.1).

Further south along the Antarctic coast, the I07S section crosses the westward flowing Antarctic Slope Front (not shown in Fig. 1). Considering data from a transient tracer section across the Weddell Gyre, Meredith et al. (2000) predicted the existence of a deep water source at around 75°E, upstream of the Antarctic Slope Front. Later, Ohshima et al. (2013) identified a deep water source near Cape Darnley (Fig. 1). Turning to numerical simulations, we find that a tracer ("brine") release experiment by Kusahara et al. (2017) has shown that the bottom water in the Enderby Basin is mostly from the Cape Darnley Polynya. Initially, the tracer spread westward over the continental shelf; it then circulates the Weddell Gyre before continuing equatorward into the Crozet Basin. There also appeared to be a direct path from Cape Darnley to the Crozet Basin (Fig. 10d of Kusahara et al., 2017). The direct spread of fresh Cape Darnley Bottom Water (CDBW) to the Enderby Basin is consistent with the result of mixing budget analyses using near-bottom hydrographic data by Aoki et al. (2020a) and Gao et al. (2022). This behaviour of the bottom water is also consistent with the observed property distribution (Fig. 8b of Orsi et al., 1999); the temperature-salinity characteristics at bottom water densities was much fresher within the longitude band of 30°E to 60°E than those within 60°E to 90°E. In Section 4.2, we estimate the mixing ratio of Cape Darnly Bottom Water and Weddell Sea Deep Water.

This paper discusses three distinct topics derived from one data set;

1. Overview of the hydrographic features with a focus in conspicuous fronts (Section 3).

2. Isopycnal diffusivity that quantifies the diffusive nature of the circulation in the deep Enderby Basin (Section 4.1).

3. Composition of AABW in the Enderby Basin (Section 4.2.)
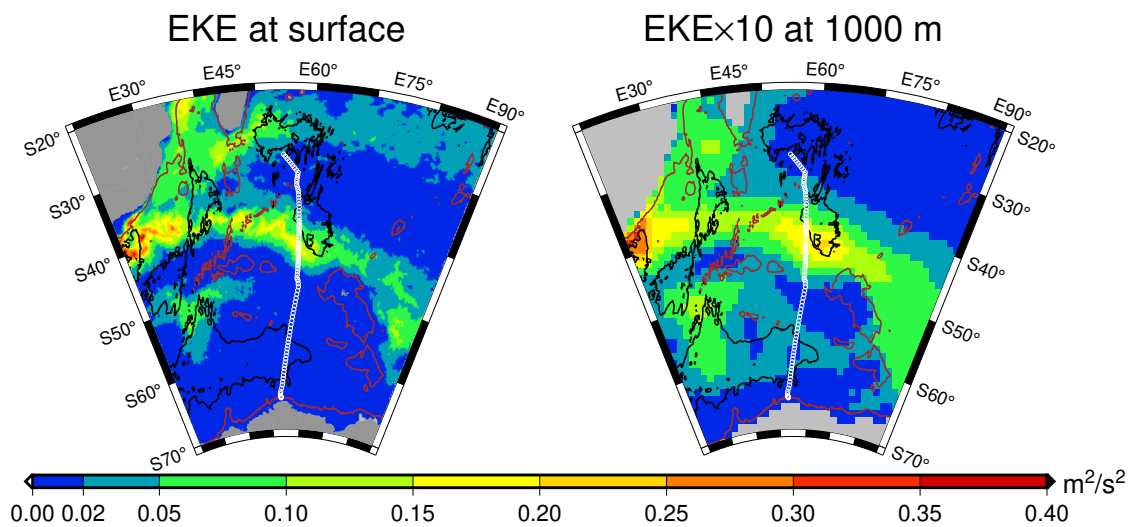
Figure 2. Eddy kinetic energy (EKE) at the surface (left) and at 1000 dbar depth (right). Note that the 1000 dbar EKE (right) is multiplied by a factor of 10. The surface EKE was estimated from geostrophic velocity anomalies of the altimetry data on a 0.25° grid. Values at 1000 dbar were estimated from the Scripps Argo float drift data on a 1° grid. The mean field was defined as the spatial and temporal average within a circle of radius 300 km with the centre at the grid point. See Katsumata (2017) for details of the EKE calculation at 1000 dbar. Black and brown bathymetry contours indicate 5000 m and 2000 m depth, respectively.

60 These three topics are preceded by a data description (Section 2) and followed by a conclusion (Section 5). The three topics are only loosely interdependent.

Eleven stations were reoccupations of previous stations at which high-precision hydrographic data had been obtained. The observed changes since the previous occupation are summarised in Appendix.

2 Data

65 The primary data used here are from conductivity, temperature, and depth profiler (CTD) and bottle measurements made onboard R/V *Mirai* during the cruise from 31 December 2019 (first station 70 at 29.5°S) to 22 January 2020 (last station 153 near seasonal ice edge at 65.3°S), nominally along 55°E (Uchida et al., 2021). The station numbers used in this work are the original station numbers found in the summary file (https://cchdo.ucsd.edu/data/14953/49NZ20191229su.txt). By using the reference thermometer (SBE35) and bottle data, the CTD data comply the GO-SHIP standard accuracies of 0.002°C
70 (temperature), 0.002 $\mathrm{g/kg}$ (salinity), and 1% (dissolved oxygen) (Hood, 2010). Standard methods were used for bottle data analysis; the Winkler method for oxygen (0.15% uncertainty), the optical methods by auto-analyzer for nutrients utilising certified materials (mean coefficient of variance less than 0.2% for nitrate, silicate and phosphate), and the chromatography for transient tracers (precision for duplicate sampling less than 0.009 $\mathrm{pmol/kg}$ for CFC12 and 0.014 $\mathrm{fmol/kg}$ for SF_6). The detail is found in Uchida et al. (2021). Expendable CTDs (XCTDs) were used for two purposes; one was to attempt resolving frontal
75 structures and the other was to replace CTD casts cancelled due to bad sea state (between 54.5 and 56°S). The depth-dependent biases of XCTD data were removed by 7 side-by-side CTD casts (Uchida et al., 2011). The manufacturer's specification of the accuracy of the XCTDs is 0.03 $\mathrm{mS/cm}$ for conductivity and 0.02°C for temperature. A pair of lowered Acoustic Doppler Current Profilers (LADCP) – one looking upward and the other downward – was used simultaneously. All eight beams from the two LADCPs worked through all casts and the signal reception was good with an average echo intensity of 56 counts for
80 all measurements, correlation of generally greater than 100 counts.

We also use data from two other GO-SHIP sections across the ACC; one section is located to the south of Africa along 30°E (section I06S), and the other crosses the Princess Elizabeth Trough nominally along 84°E (section I08S). Data collected at several stations during cruises of M/V *Marion Dufresne* (MD43, MD68, and MD75) and GO-SHIP I05 were used for decadal comparisons (see Appendix). CTD and bottle data from the latest cruises of R/V *Hakuho* near Cape Darnley (KH19 and KH20)
85 were also used. The cruises are listed in Table 1. Additionally, gridded sea surface altimeter data from the Copernicus Marine Service and Argo float drift data from the Scripps Institution of Oceanography were used (see Data Availability section). To denote density, we use γ^n notation where $\gamma^n = 26.8$ means a neutral density (Jackett and McDougall, 1997) of 1026.8 $\mathrm{kgm^{-3}}$.

3 Fronts

Park et al. (1991, 1993) defined four fronts that they observed in the Crozet Basin by their hydrographic characteristics at 200
90 dbar depth (Fig. 3). These front definitions as they apply to the I07S section are summarised in Table 2, which also lists the
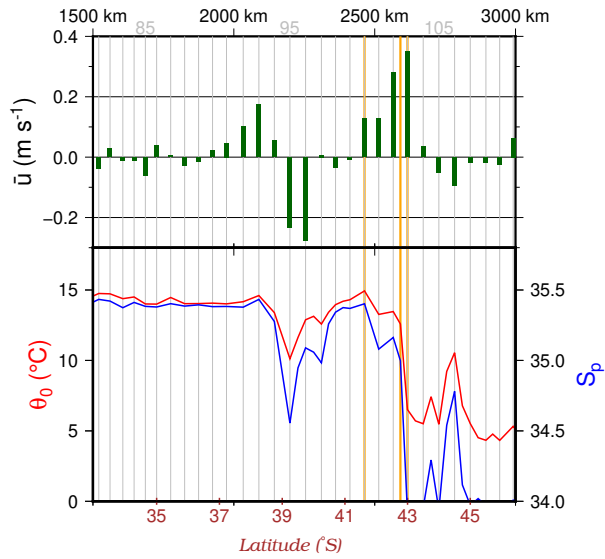
Figure 3. Zonal velocity averaged over the water column ($\overline{u}$, upper panel), and potential temperature (θ_0, red) and practical salinity (S_p, blue) at 200 dbar depth. The zonal velocity is positive eastward. The traditional potential temperature and practical salinity scale are used in this figure to facilitate comparison with previous publications. The horizontal axes are distance X (upper) as in Fig. 4 and latitude (lower) The vertical grid lines indicate the location of the CTD stations (does not include XCTD stations) with station numbers shown on the upper horizontal axis in grey. The vertical orange lines show estimated approximate positions of the Agulhas Return Current front, Subtropical front, and Subantarctic front (from north to south).

Table 1. Cruises. The cruises for sections I07S, I07N, I06S, I08S, and I05 are under the Global Ship-based Hydrographic Investigation Program (or its predecessor World Ocean Circulation Experiment). KH19 and KH20 are cruises onboard R/V *Hakuho* (Ohashi et al., 2022). Others are cruises onboard M/V *Marion Dufresne* (e.g. Park et al., 1991).

Section	Cruise duration	`Expo code` or PROJECT
I07S	Dec 2019 – Feb 2020	49NZ20191229
I07N	Apr 2018 – Jun 2018	33RO20180423
I06S	Apr 2019 – May 2019	325020190403
	Feb 2008 – Mar 2008	33RR20080204
	Feb 1996 – Mar 1996	35MF103_1
	Feb 1993 – Mar 1993	35MFCIVA_1
I08S	Feb 2016 – Mar 2016	33RR20160208
	Feb 2007 – Mar 2007	33RR20070204
	Dec 1994 – Jan 1995	316N145_5
I05	Mar 2009 – May 2009	33RR20090320
	Mar 2002 – Apr 2002	74AB20020301
	Nov 1987 – Dec 1987	74AB29_1
KH19	Jan 2019 – Feb 2019	–
KH20	Jan 2020 – Feb 2020	–
74DI	Mar 1994	74DI207
MD43	Mar 1985	INDIGO
MD68	Apr 1991	SUZIL
MD75	Apr 1993	ANTARES

major southerly fronts defined by Orsi et al. (1995). The Southern ACC Front is found at around 62.5°S. At around 64.8°S, the Southern Boundary of the ACC passes over the continental slope at about 3000 dbar depth. These locations are consistent with those reported in Williams et al. (2010) who indicated that the Weddell Gyre is limited to the area west of Cape Ann. Hydrographic sections of temperature, salinity, and dissolved oxygen are shown in Fig. 4. The station interval of 30 nautical

95 miles (15 nm with XCTD) was found to be insufficient to separate the Subtropical and Subantarctic fronts. The low salinity and low temperature anomaly centred at 39°S (about $X =$2200 km) is a cyclonic (negative sea surface height anomaly) eddy, not a front. As seen in Fig. 5, our observation track passed very close to the eddy's centre, and the upward heave of isotherms and isohalines are striking. The ACC fronts are found located around 41°S to 43°S, ($X =$2400 to 2600 km) (Fig. 5). The three northern fronts are accompanied by a strong eastward jet with a vertically averaged velocity > 0.1 ms^{-1} but the jet along the

100 Polar Front is weaker at < 0.03 ms^{-1}. Comparison of two snapshots obtained 4 days apart (Fig. 5) demonstrates that some eddies near the front (e.g., around 57.5°E, 43.5°S) were advected eastward, whereas others (e.g., 58°E, 39°S) moved westward, in agreement with the description by Park and Gambéroni (1997) that "even a section made in a few days across the frontal zone might not be considered as synoptic".
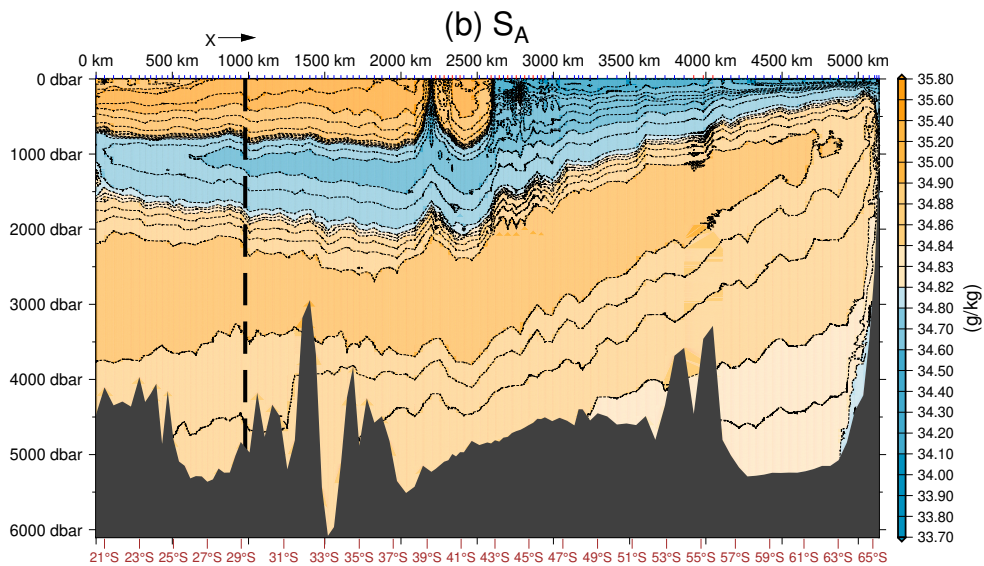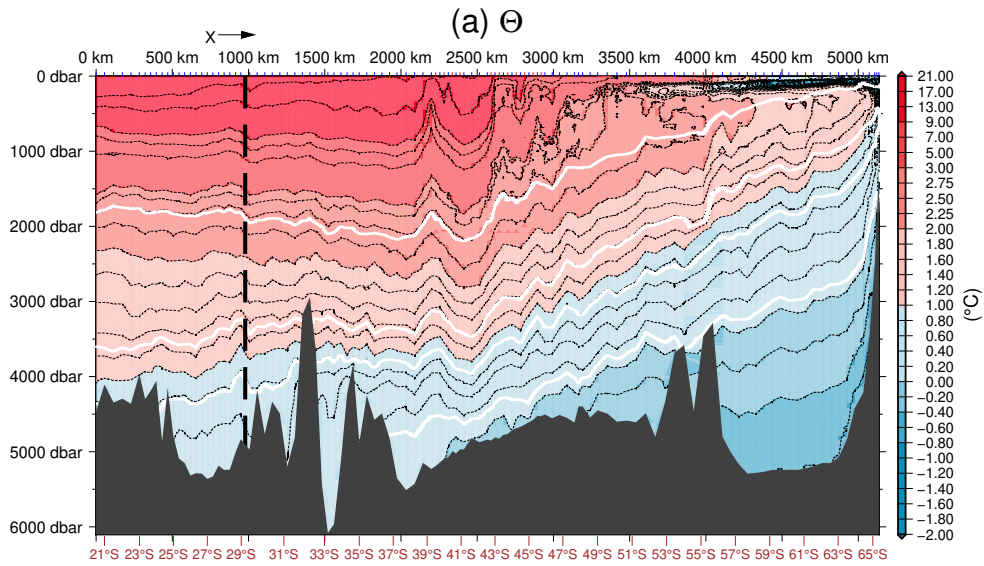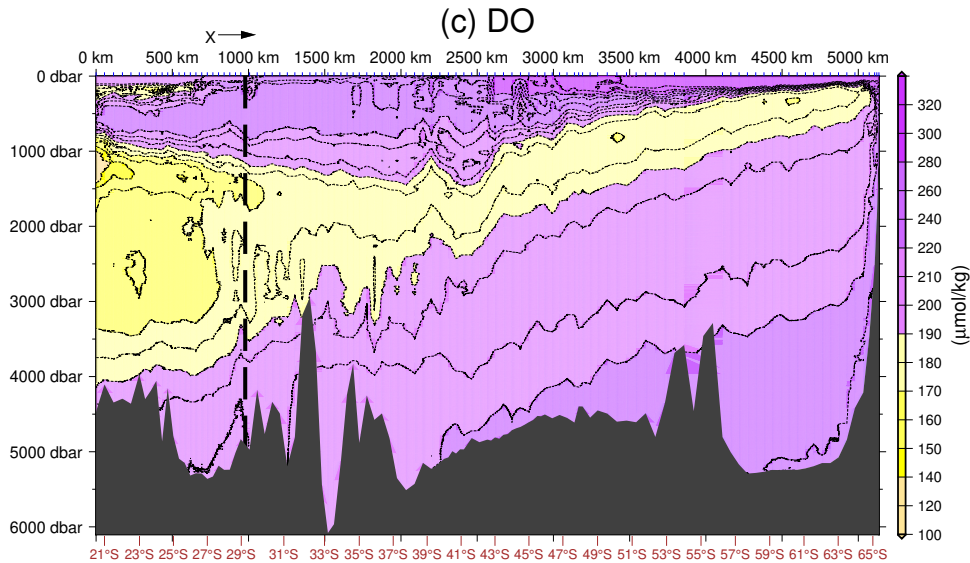
Figure 4. (a) Conservative Temperature Θ (°C), (b) Absolute Salinity S_A (g kg^{-1}), and (c) dissolved oxygen (μmol kg^{-1}) observed along the I07 section. The section north of 29.5°S (vertical dashed line) was occupied from April to May 2018 during cruise 33RO20180423, and that south of 29.5°S was occupied from December 2019 to January 2020 during cruise 49NZ20191229. The upper horizontal axis shows the distance (X) from Station 26 of cruise 33RO20180423 at 54.517°E, 20.502°S. The corresponding latitudes are denoted in the lower axis with brown ticks and labels. The blue and red ticks on the upper horizontal axis show the position of CTD and XCTD casts, respectively. The vertical axis shows pressure. In (a), the white contours indicate neutral densities of $\gamma^n = 27.9, 28.11, 28.18$, and 28.27.

The slopes of the isohaline and isotherms at the fronts are steep: $S_A = 34.82$ g/kg isohaline is at 560 dbar at $X = 2591.2$
105   km and it crops out north of the next station at $X = 2616.4$ km, whereas the $\Theta = 9°$C isotherm jumps from 555 dbar to 45 dbar between these stations. Both have a slope of 2×10^{-2}. Because the meridional gradients of temperature and salinity are density compensating, the slope of the corresponding isopycnal is smaller (506 to 271 dbar or 0.2×10^{-2}).

The steep salinity front can be explained by surface forcing. The meridional gradient of surface salinity in the climatological data set (Reagan et al., 2024) across these fronts (Fig. 6) is the strongest in the Southern Hemisphere. In such climatological
110   data, the stationarity of the fronts also likely contributes to its large gradient. Strong evaporation in the midlatitude Indian Ocean results in salty surface mixed layer. The salty surface water mass is advected by the Agulhas Current and returns in the Agulhas
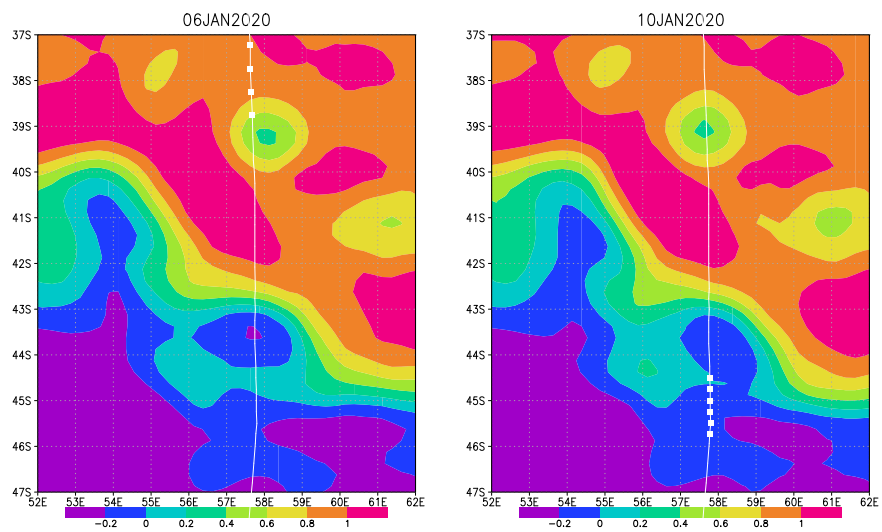
Figure 5. Two snapshots of the absolute dynamic topography; 6 January 2020 UTC (left) and 10 January 2020 UTC (right). The thin white line shows the cruise track, and the white squares show the CTD and XCTD stations occupied on each day.

Table 2. Major fronts at 55°E. The traditional potential temperature (θ_0 in °C) and practical salinity (S_p, unitless in Practical Salinity Scale) are used in this table to facilitate comparison with previous publications.

Front	θ_0 range	axial value	S_p range	axial value	station	latitude
Agulhas Return Current[a]	12–16	14	35.1–35.5	35.3	100	41.6°S
Subtropical[a]	8–12	10	34.6–35.1	34.8	102 or 103	42.5 or 43°S
Subantarctic[a]	4–8	6	34.1–34.5	34.3	103	43°S
Polar[b]	–	–	–	–	121	51°S
Southern ACC[c]	–	–	–	–	145	62.5°S
Southern Boundary[d]	–	–	–	–	150	64.8°S

a As defined by Park et al. (1991) using temperature and salinity at 200 dbar depth.

b Northern limit of subsurface potential temperature minimum of $\theta_0 = 2$°C.

c Potential temperature maximum $\theta_0 > 1.8$°C (Orsi et al., 1995).

d Potential temperature maximum $\theta_0 > 1.5$°C (Orsi et al., 1995).

Return Current to the north of the fresh ACC, which amplifies the meridional haline gradient imprinted by precipitation minus evaporation.

Using data from a limited number of stations, Park et al. (1993) mapped dissolved oxygen at 3000 dbar depth (their Fig. 11) and found a frontal structure between 57°E, 32°S and 75°E, 43°S, separating low-oxygen North Indian Deep Water (NIDW) to the northeast from oxygen-rich Lower Circumpolar Deep Water (LCDW) to the southwest. Across the front, strong isopycnal mixing of NIDW and LCDW was inferred from the water properties. Our section (Fig. 4c) crosses the front at around 28°S (which was observed as part of I07N) showing the corresponding mesoscale structures north of 33°S at around 3000 dbar depth. The horizontal currents measured by LADCP appeared turbulent (not shown). This feature supports the inference by Park et al. (1993) that isopycnal mixing is strong across the front.

4 Deep circulation in the Enderby Basin

A snapshot of the horizontal circulation in the deep Enderby Basin is examined by plotting the LADCP data (Fig. 7). As suggested by the mean velocities, which are well within the variance ellipses, there is no obvious large-scale background flow. As the mesoscale wiggles of the sea surface height contours suggest, the field is characterised by numerous eddies, and our snapshot observation could not capture any mean transport. The eddies imply that the circulation in the deep Enderby Basin is diffusive in nature. It is possible to estimate vertical diffusivity from LADCP and CTD data by using a finescale internal wave parameterisation as is discussed in detail by Sasaki et al. (2024). We found that vertical diffusivity in the deep Enderby Basin is moderately strong (10^{-5} to 10^{-4} m^{2}s^{-1}) and is enhanced towards the bottom. Using this vertical diffusivity, we attempted to estimate the horizontal diffusivity from the spatial distribution of transient tracers.

Meridional gradient of surface salinity
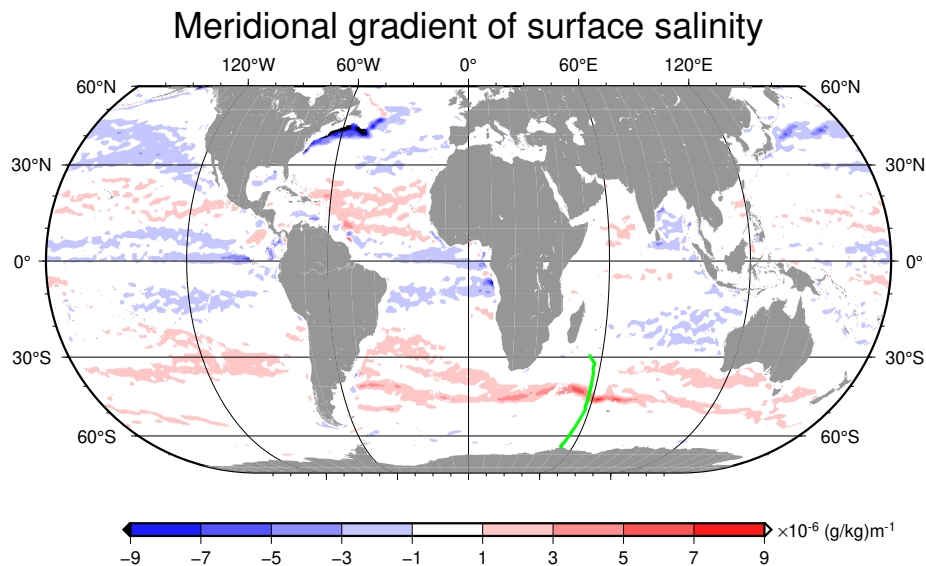
Figure 6. Meridional gradient of surface salinity from the World Ocean Atlas 2023 (Reagan et al., 2024). The meridional gradient was calculated from the gridded salinity product on a $\frac{1}{4}$-degree grid. Large cross-shore gradients in coastal regions are avoided by restricting the plot to ocean depths > 3000 m. The Arctic Ocean is also excluded. Green dots indicate the I07S stations.

4.1 Isopycnal diffusivity estimated from transient tracer distributions

Four kinds of transient tracers were measured along I07S. Here, we used CFC12 and SF_6 because CFC12 has had the highest atmospheric concentration since the 1970s and because time evolution of SF_6 is quite different from that of CFC12.

As mentioned above, no obvious background flow was observed. Without any advecting mean flow, the concentration of a tracer in a meridional section $c(y, z, t)$ is governed by

$$\frac{\partial c}{\partial t} = K \frac{\partial^2 c}{\partial y^2} + D \frac{\partial^2 c}{\partial z^2}, \tag{1}$$

where t is time; the direction of y and z are northward along the isopycnal surfaces and across the isopycnal surfaces (positive towards the lighter density), respectively (McDougall, 1984); K is isopycnal diffusivity; and D is diapycnal diffusivity. Spatial and temporal variations of K and D are neglected. If we scale time by T, horizontal distance by $\sqrt{KT}$, and vertical distance
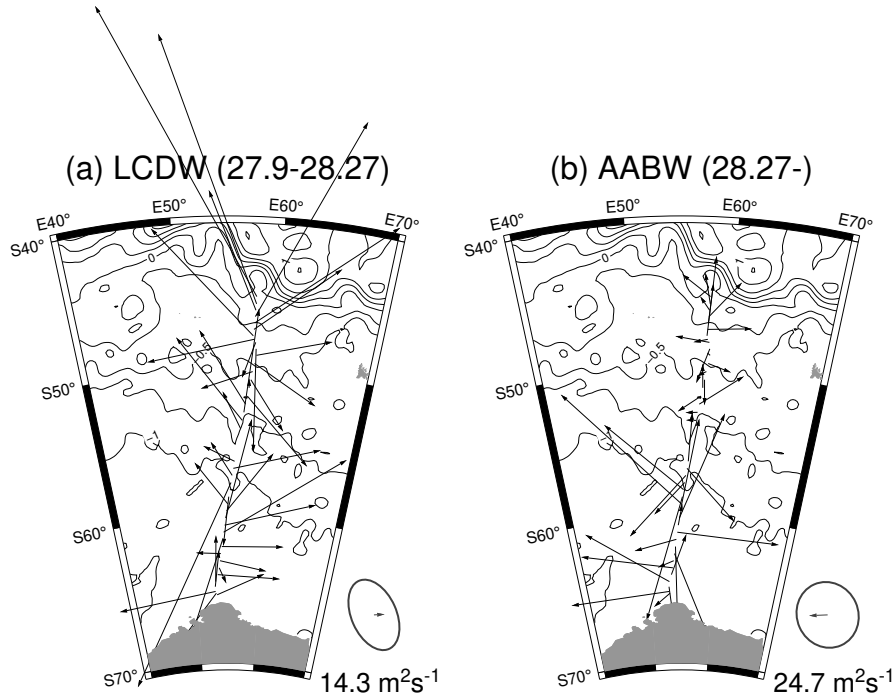
Figure 7. Instantaneous velocity observed by LADCP. (a) Horizontal velocity averaged within the LCDW layer ($27.9 < \gamma^n < 28.27$) and (b) within the AABW layer ($28.27 < \gamma^n$). The contours with intervals of 0.25 m (thin) and 0.5 m (thick, labelled) show the absolute sea surface height (SSH) field averaged over the cruise period (31 December 2019 to 22 January 2020). The SSH data are from satellite altimetry. The variance (ellipses) and mean (vectors) of the horizontal velocity in the Enderby Basin (defined here as south of $56°$S) are shown at the right bottom corner of each panel. The vectors also give the scale.

by $\sqrt{DT}$, the equation becomes simply

$$140 \qquad \frac{\partial c}{\partial t} = \frac{\partial^2 c}{\partial y^2} + \frac{\partial^2 c}{\partial z^2}. \qquad (2)$$

Profiles of the tracers (Figs. 8b and 8e) clearly show that dense shelf water with high tracer concentrations flows along the continental slope of Antarctica. We approximate this slope as a vertical wall and model this situation by considering two time-dependent tracer sources: one is a point source at the bottom of the slope and the other is a line source placed along the southern vertical wall. It might be that the possible deep eastern boundary current along the western flank of the Kerguelen
145 Plateau injects additional tracers, but this effect cannot be included in our meridional two dimensional model and we regard this effect as part of the uncertainty. The point source represents young dense water masses carried westward by the Antarctic Slope Current, possibly including some contribution from the Australia Antarctic Basin through the Princess Elizabeth Trough, whereas the line source is the newly ventilated water flowing along the continental slope. In neutral density coordinates (Figs.

8a and 8c), the point source is at $(y, z) = (0, 0)$ and the line source is at $y = 0$. We designate tracer distribution originating from the point source as c_0 and that originating from the line source as c_1 and seek a solution as their superposition;

$$c(y, z, t) = \alpha_0 c_0(r, t) + \alpha_1 c_1(y, t), \tag{3}$$

where α_0 and α_1 are constants to be determined. The solution $c_0(r, t)$ is governed by (2) and is given in cylindrical coordinates with $r = \sqrt{y^2 + z^2}$:

$$\frac{\partial c_0}{\partial t} = \frac{1}{r} \frac{\partial c_0}{\partial r} + \frac{\partial^2 c_0}{\partial r^2}, \tag{4}$$

with the boundary conditions

$$c_0(r = 0, t) = s_0(t - \delta_0) \tag{5}$$
$$\frac{\partial c_0(y = 0, t)}{\partial z} = \frac{\partial c_0(z = 0, t)}{\partial y} = 0,$$

where the time offset δ_0 is the advection time from the surface mixed layer to the I07S section, and s_0 is the source of the tracer as a function of time. The solution $c_1(y, t)$ is governed by

$$\frac{\partial c_1}{\partial t} = \frac{\partial^2 c_1}{\partial y^2}, \tag{6}$$

with the boundary conditions

$$c_1(y = 0, t) = s_1(t - \delta_1) \tag{7}$$
$$\frac{\partial c_1(y = 0, t)}{\partial z} = 0,$$

where δ_1 is, again, the advection time, which can be different from δ_0, and s_1 is the source function. The sum $\alpha_0 c_0 + \alpha_1 c_1$ only approximately satisfies the boundary condition at the southern boundary $y = 0$, which is a limitation of this model. The governing Eqs. (4) and (6) were numerically solved with realistic source functions $s_0(t)$ and $s_1(t)$. We take the unit time as $T = 1$ year. Calculations were carried out for the year 1950 to 2020 with a non-dimensional grid spacing of 0.1 for $0 < r < 50$ and $0 < y < 50$. The source functions reflect the atmospheric concentration of the tracers, which is converted to the concentration within the mixed layer by laboratory-determined solubility (Warner and Weiss, 1985; Bullister et al., 2002) at an assumed seawater temperature of $0°C$, salinity of 34.5 practical salinity, and a constant saturation rate. A typical observed saturation rate is 70% (Schlosser et al., 1991; Ohashi et al., 2022), but the tracers in the dense shelf water are diluted when they form the source water at depth. We tested saturation rates between 35% and 70% and found an overall error similar to that for saturation rates between 50% and 70%, but greater for smaller saturation rates. We therefore use a saturation rate of 50% here. The atmospheric concentration before 2015 is taken from Bullister and Warner (2017) and that after 2015 from the NOAA Global Monitoring Laboratory, following Ohashi et al. (2022).

Nonlinear least squares fit of Eq.(3) (Levenberg-Marquardt method, Madsen et al. (2004)) was used to find the values of α_0, α_1, δ_0, δ_1, and K that minimise the difference between the predicted and observed concentration of CFC12 and SF_6.

In the calculation of this difference, the source area was excluded by limiting the comparison to observed concentrations of $< 0.4 \text{ pmolkg}^{-1}$ for CFC12 and $< 0.21 \text{ fmolkg}^{-1}$ for SF_6; thus we fit Eq.(3) to 125 and 118 bottle data for CFC12 and

180 SF_6, respectively. To estimate the isopycnal diffusivity K, we used the fixed diapycnal diffusivity of $D = 4.7 \times 10^{-5} \text{ m}^2\text{s}^{-1}$ which is the arithmetic mean of the diapycnal diffusivity below 2000 dbar between 56°S and 63.5°S estimated by finescale parameterisation (Polzin et al., 2014) of the observed stratification and horizontal velocity field (Katsumata et al., 2021). The observed diapycnal diffusivity showed some spatial variability (Fig. 8c) and the diffusivity is high where the near-bottom CFC12 concentration is high ($Y = 400$ to 700 km in Fig. 8a and b). We neglect this spatial variability. Next, we prescribe

185 a set of initial values, namely, at $\alpha_0 = 0.1, \alpha_1 = 0.1$, and $K = 500 \text{ m}^2\text{s}^{-1}$ for fitting by the Levenberg-Marquardt method. The advection times δ_1, δ_0 are each set at 0, 1, $\cdots$ 19 years, giving 400 combinations of δ_1 and δ_0 for the nonlinear least squares calculation; thus we obtain 400 sets of α_1, α_2, and K. We tried several different sets of initial values (for example $K = 100 \text{ m}^2\text{s}^{-1}$) but they converged to the same solution. The error did not show an obvious sharp global minimum. The global minimum error (sum of squares) was 0.117 for the 400 set of trials and the error histogram (not shown) is a decreasing

190 function of the error with a change of the decreasing slope at error $= 0.25$. We thus selected the 160 parameter sets with error < 0.25 as good estimates. The averages and standard deviations of the good estimates are $\delta_0 = 10 \pm 6$ years, $\delta_1 = 16 \pm 3$ years, $\alpha_0 = 0.12 \pm 0.04$, $\alpha_1 = 0.14 \pm 0.01$, and $K = 72 \pm 16 \text{ m}^2\text{s}^{-1}$. We note that this uncertainty does not include the contribution due to the simplification introduced in our crude model such as spatial variability of the diapycnal diffusivity D and temporal change of source saturation rate. These mean values are used in Fig. 8. The "age" of the source water (δ_0 and δ_1) appears to be

195 overestimated compared with ages obtained by other methods e.g. Ohashi et al. (2022); possible reasons include the saturation uncertainty or a limitation due to the idealised source function.

The estimated isopycnal diffusivity of $K = 72 \pm 16 \text{ m}^2\text{s}^{-1}$ is not much different from past estimates in deep seas. For example, the isopycnal diffusivity at 4000 dbar in the Atlantic Ocean has been estimated by an artificial tracer release experiment to be about $100 \text{ m}^2\text{s}^{-1}$(Ledwell, 2024). Phillips and Rintoul (2000) have estimated horizontal temperature diffusivity near

200 the Subantarctic front, South of Australia, to be 100 to $200 \text{ m}^2\text{s}^{-1}$ at 2240 dbar and 3320 dbar. Our value is also similar to the isopycnal diffusivity on the continental rise in the Antarctic Australia Basin (Katsumata and Yamazaki, 2023) and a deep diffusivity of 30 to $70 \text{ m}^2\text{s}^{-1}$ estimated by a plume model of AABW based on observation of transient tracers in the Weddell Sea (Haine et al., 1998). The diffusive nature of the interior circulation also agrees with the CFC distribution in Fine et al. (Fig. 5 of 2008) with sparce contours in the interior of the Enderby Basin compared to packed contours found in near-boundary

205 regions. The tracer distribution thus suggests that circulation in the deep Enderby Basin is mostly dominated by the westward transport near the Antarctic slope and isopycnal interior diffusion. The diffusivity value is typical of that for deep basins, where values are weaker than those observed in the upper water column (500 to $1000 \text{ m}^2\text{s}^{-1}$), e.g. Tulloch et al. (2014).

4.2 AABW composition

The Enderby Basin collects AABW from four major sources – Weddell Sea Deep Water (WSDW), Cape Darnley Bottom Water

210 (CDBW), Adélie Land Bottom Water (ALBW), and Ross Sea Bottom Water (RSBW). WSDW arrives at the I07S section from the west, while ALBW and RSBW flow through the Princess Elizabeth Trough further to the east (Heywood et al., 1999).
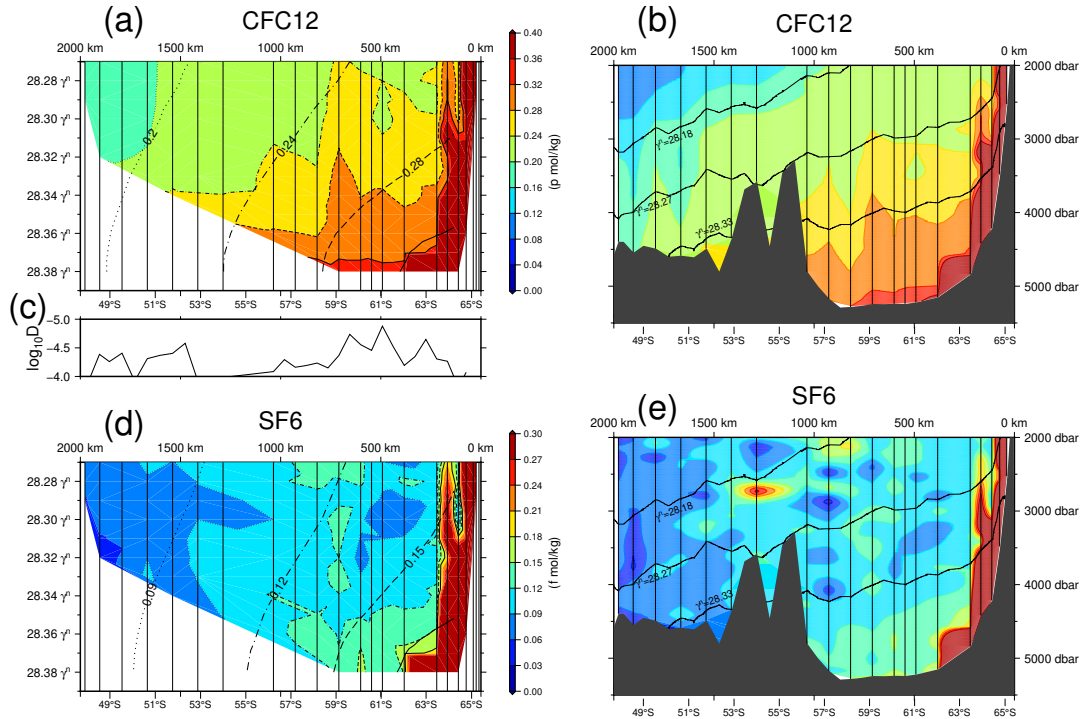
Figure 8. Concentrations of transient tracers (a, b) CFC12 and (d, e) SF_6. The horizontal axes show latitude (bottom) and distance (Y, top) from the southernmost station, and the vertical axis shows density in (a) and (d) and pressure in (b) and (e). The colours in (a) and (b) show the concentration of CFC12 in pmolkg^{-1}, whereas those in (d) and (e) show the concentration of SF_6 in fmolkg^{-1}. The contours in (a) and (d) show the concentrations predicted by the simple diffusion model (3) with $\alpha_0 = 0.12$, $\delta_0 = 10$, $\alpha_1 = 0.14$, and $\delta_1 = 16$. The same type of contour lines are used for observed and predicted quantities. The contours in (b) and (e) show the isopycnals $\gamma^n = 28.18, 28.27$, and 28.33. The observed concentrations in the pressure vertical coordinate in (b) and (e) are converted to density vertical coordinate in (a) and (d). (c) shows diapycnal diffusivity D averaged below $2000\,\mathrm{dbar}$.
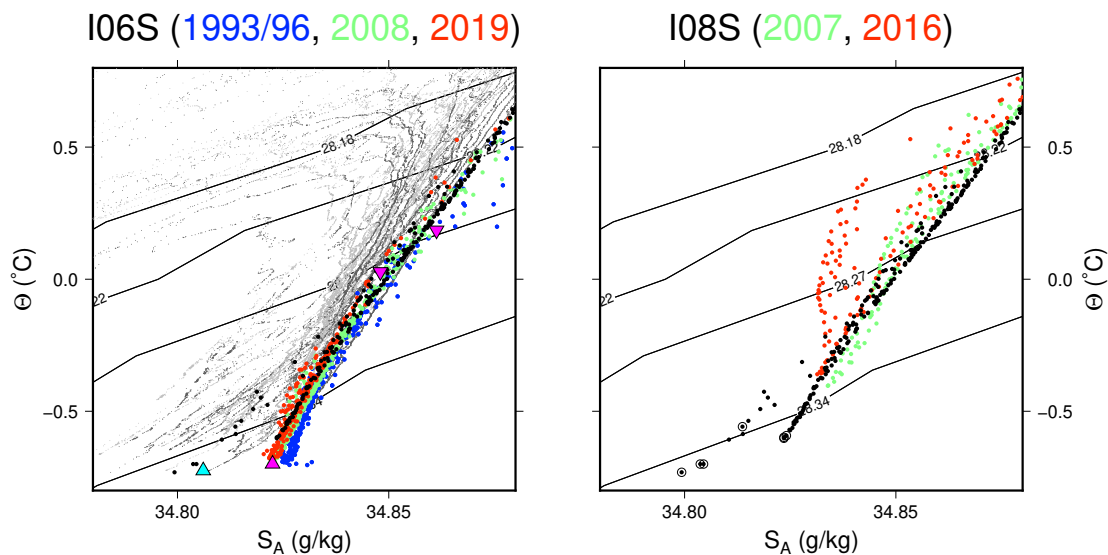
Figure 9. Temperature-salinity diagrams of the bottom waters at 30°E (I06S, left) and at 82°E (I08S, right) based on data from different occupation years (indicated by the colours of the circles). Black points show the data of I07S observed in 2019/20, and the dark and light grey points show data of R/V *Hakuho* (KH) cruises in 2019 and 2020, respectively (see Fig. 1). For I06S, only bottle data collected at depths with density $\gamma^n > 28.0$ are shown. For I08S, only bottle data from south of 60°S at depths with density $\gamma^n > 28.0$ and deeper than 1000 dbar are shown. For I07S, only bottle data at depths with density $\gamma^n > 28.0$ and deeper than 3000 dbar are shown. In the right panel, data points for the deepest bottles (i.e. 10 m above the seafloor) and south of 60°S along the I07S section (black points) are circled. The source waters used in the mixing analysis are indicated by triangles; inverted magenta triangles, LCDWs ($S_A = 34.86$ g/kg, $\Theta = 0.19°$C; $S_A = 34.85$g/kg, $\Theta = 0.03°$C); magenta triangle, WSDW ($S_A = 34.82$ g/kg, $\Theta = -0.70°$C); and cyan triangle, CDBW ($S_A = 34.81$ g/kg, $\Theta = -0.72°$C). Density contours $\gamma^n = 28.18, 28.22, 28.27,$ and 27.34 are shown.

Previous occupations of GO-SHIP Sections I06S at 30°E and I08S at 85°E provide information on how WSDW and ALBW+RSBW each contribute to AABW at I07S (Fig. 9). On the temperature-salinity diagram, points for upper AABW ($28.18 < \gamma^n < 28.33$) on I08S are scattered (Fig. 9) because these densities on the shelf are subject to direct atmospheric forcing. The deep water masses are, however, similar to I07S within the AABW range ($28.27 < \gamma^n < 28.34$). Menezes et al. (2017) have reported freshening of bottom water in the Princess Elizabeth Trough. On I06S, points for the lighter water masses

$\gamma^n < 28.22$ are similarly scattered. On I06S below $\gamma^n = 28.22$, persistent freshening from 1993 to 2008 is discernible and the water on I07S appears to be in between the 2008 and 2019 water masses observed along I06S. Haine et al. (1998), using CFCs, estimated the mean transient time from the Greenwich meridian ($0°$E) to the Crozet-Kerguelen gap ($55°$E) along the southern flank of the Southwest Indian Ridge as 12 to 20 years (their Fig. 5) depending on the diffusion assumptions adopted. The transient time between $30°$E and $55°$E is likely half that, i.e., 6 to 10 years. We therefore use the 2008 observations on I06S as the source water in our mixing model.

We note that the bottom water on I08S was not dense enough to explain the near-bottom water (> 28.34) observed at I07S. We thus conclude that the densest class of AABW ($\gamma > 28.34$) observed on I07S is a mixture of WSDW and CDBW.

Orsi et al. (1999) called the water mass with $28.18 < \gamma^n < 28.27$ "ACC Bottom Water" (ACCbw) because it is well mixed and showing little zonal variability compared to the water masses above or below. The focus in this section is thus on water masses deeper than $\gamma^n = 28.27$, which fill the Enderby Basin and south of $39°$S, the Crozet Basin (Fig. 4a). Here we estimate the composition of AABW ($\gamma^n > 28.27$) in the Enderby Basin using a method following that used in Johnson (2008), i.e. least squares fitting with a non-negative constraint in which temperature, salinity, $PO^* = 170[PO_4] + [O_2]$, $NO^* = 10.625[NO_3] + [O_2]$, and $SO^* = 1.66[SO_4]+[O_2]$ are conserved. The method yields six equations (one being mass conservation). We do not expect potential vorticity be conserved because the flow is subject to bottom friction. The weights for the conservation equations are taken from Johnson (2008); 1, 0.25, 1, 0.5, 0.5, and 0.25 for mass, temperature, salinity, PO^*, NO^*, and SO^*, respectively. As reflected in their relatively small weights, the pseudo-tracers, PO^*, NO^*, and SO^*, do not provide strong constraints as manifested by the almost linear distribution of the data points when they are plotted against temperature (Appendix, Fig.B1).

The number of the unknowns (source water masses) is four; two are CDBW and WSDW, and LCDW which overlies these AABW is expressed by the linear combination of two extremes (warm/salty and cold/fresh), which we call LCDW1 and LCDW2. It is possible that the bottom waters from the Ross Sea (RSBW) and Adélie Land (ALBW) cross the I07S section after flowing through the Princess Elizabeth Trough, but some previous studies have suggested otherwise. A numerical simulation by Kusahara et al. (2017) indicates that bottom waters that have passed through Princess Elizabeth Trough form a deep eastern boundary current flowing along the west coast of the Kerguelen Plateau, that is, eastward from $60°$E (their Figs. 8a and 8b) and do not spread into the Enderby Basin. Aoki et al. (2020a) also reported that south of $62°$S near the bottom (within 300 dbar of the seabed), influences by RSBW and ALBW were discernable only at $70°$E and not at $60°$E. We therefore neglect the contributions from ALBW and RSBW to the interior Enderby Basin. We expect that LCDW originates mostly from the upstream ACC. As seen in Fig. 9, LCDW in the interior Enderby Basin is not a homogeneous water mass but shows a range of temperature and salinity. We thus chose two end points and express the range as the mixing (linear combination) of these two. One end point is Station 31 ($42.5°$E, $30°$S) depth 4670 dbar ($\gamma^n = 28.265$), and the other is Station 50 ($52.0°$E, $30°$S) depth 3210 dbar ($\gamma^n = 28.279$). For WSDW, we use data from the bottom (5245 dbar) bottle at Station 71 ($\gamma^n = 28.4$) from the 2008 I06S occupation. CDBW is represented by the C03 station of the KH19 cruise, $61.81°$E $63.1°$S, sampling depth 4542 dbar ($\gamma^n = 28.394$), because the water properties there ($S_A = 34.81$ g/kg, $\Theta = -0.72°$C) are closest to the average value for CDBW measured by a year-long mooring ($S_A = 34.807$ g/kg, $\Theta = -0.777°$C when converted to the TEOS-10 value) near Cape Darnley (Ohshima et al., 2013).
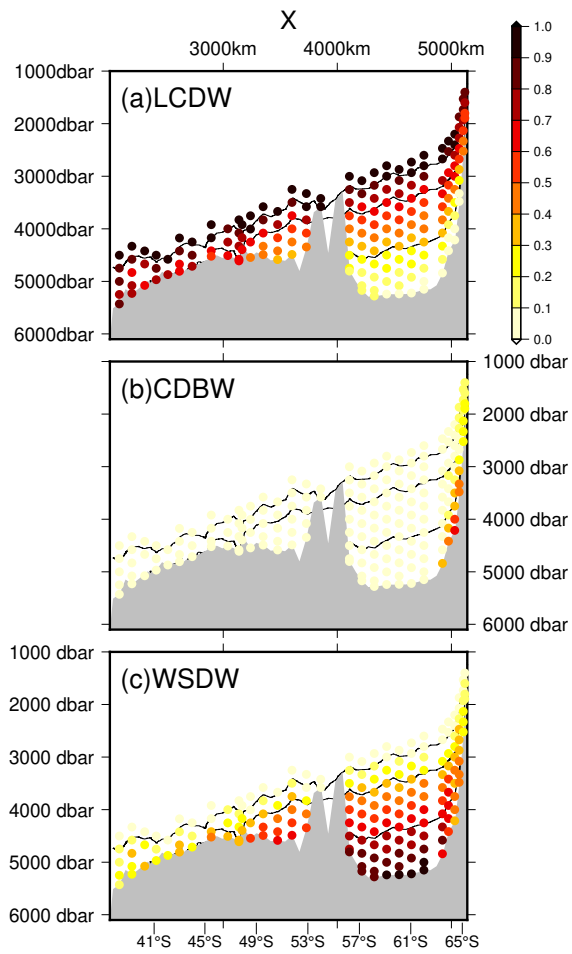
Figure 10. Mixing ratio of sources for Antarctic Bottom Water in the Enderby and Crozet Basins along the I07S section. The upper horizontal axis shows distance, X, the bottom axis shows approximate latitude. The vertical axis shows pressure. The contours are isopycnals at $\gamma^n = 28.27, 28.30$ and 28.35.

The mixing ratios in Fig. 10 show some scatter, but the overall composition of AABW varies roughly with density. On $\gamma^n = 28.27$, CDBW=0% to 20%, WSDW=5% to 35%, and LCDW=LCDW1+LCDW2=70% to 95%. The contribution changes approximately linearly towards $\gamma^n = 28.35$ where CDBW=0% to 35%, WSDW=35% to 75%, LCDW=25% to 45%. As expected from the closeness of the I07S temperature and salinity to those of I06S (Fig. 9, left), AABW in the Enderby Basin consists mostly of WSDW with little contribution from CDBW. Near the shelf ($X > 5000$ km, south of 63°S), near-bottom water mass shows considerable contribution from CDBW, as indicated by several isolated relatively fresh points on the temperature-salinity diagram (Fig. 9).

We examined the sensitivity of the results to the choice of source water masses. For WSDW, Station 70 (30.0°E, 62.0°S, 5267 dbar), Station 69 (30.0°E, 61.5°S, 5294 dbar), Station 73 (30.0°E, 63.5°S, 5217 dbar), and Station 75 (30.0°E, 64.5°S, 5105 dbar) were substituted for the original source water at Station 69. Similarly for CDBW, C02 (59.45°E, 63.50°S, 4370 dbar), C04 (63.69°E, 64.10°S, 3922 dbar), C05 (65.20°E, 64.96°S, 3364 dbar), and C06 (66.25°E, 65.50°S, 3363 dbar) were each substituted. From these combination we obtained 25 pairs of calculations: the spreads of the results at Stations 134 ($L =4215$ km, 57.22°S), 142 ($L = 4650$ km, 61.09°S) and 148 ($L =4975$ km, 63.97°S) are shown in Fig. 11. Because LCDW is represented by the linear combination of two extremes, the sensitivity to LCDW was not examined. The estimates for CDBW and WSDW show an uncertainty of $\pm$ 20% or greater. In contrast, the estimates for LCDW show smaller spread. The uncertainty does not change the qualitative conclusion that the contribution of WSDW to the AABW in the Enderby Basin is greater than that of CDBW.

5 Conclusions

In this paper, results from a 2019 cruise along 55°E south of 30°S are delineated with emphasis on deep to bottom circulations. At 55°E, the deep to bottom circulation is primarily diffusive with no obvious mean flow – thus transient tracers show equatorward spread in accordance with the large-scale meridional gradient. In this sense, the eastern boundary of the Weddell Gyre does not reach as far east as 55°E.

Because the 2019 cruise was the first occupation of the new GO-SHIP section I07S, only 11 previously occupied stations were revisited (Table A1 in Appendix). In the present comparison, the bottom salinity "rebound" in the Australia-Antarctic Basin, which was reported to be propagating westward (Aoki et al., 2020b) was not detected. The next GO-SHIP occupation of the I07S section will measure changes in the Enderby Basin not only in temperature and salinity but also in other parameters that were sampled during the 2019 cruises, including nutrients calibrated against certified reference materials and biological parameters such as microbial diversity and abundance.

Data availability. Hydrographic data from GO-SHIP cruises are available from CCHDO (CCHDO, 2023), Hydrographic data from *Marion Dufresne* are available from SeaDataNet https://cdi.seadatanet.org/. Hydrographic data from *R/V Hakuho* are available from https://ads.nipr.ac.jp/dataset/A20240612-002 and https://ads.nipr.ac.jp/dataset/A20240613-001. The altimetry data are "Global Ocean Gridded L 4 Sea
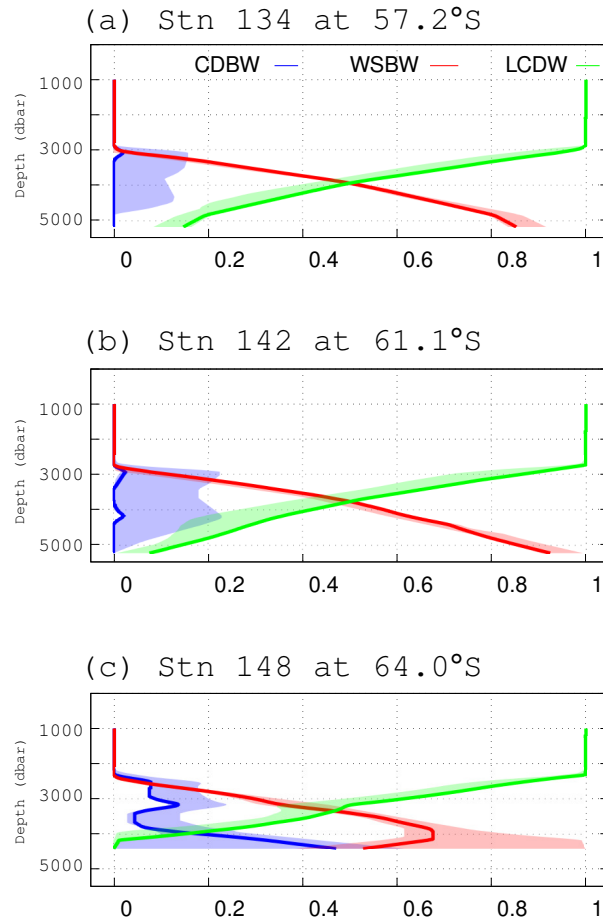
Figure 11. Vertical profiles of the estimated composition (horizontal axes) of AABW in the Enderby Basin. The contributions from Cape Darnley Bottom Water (CDBW), Weddell Sea Deep Water (WSDW), and Lower Circumpolar Deep Water (LCDW) are shown by blue, red, and green lines, respectively, and the accompanying shading shows the spread (minimum and maximum) of the estimates for 25 pairs obtained using different choices for CDBW and WSDW properties. The bottle data were vertically interpolated by the method of Reiniger and Ross (1968).

Surface Heights And Derived Variables Reprocessed 1993 Ongoing" E.U. Copernicus Marine Service Information (CMEMS), Marine Data Store (MDS), DOI: 10.48670/moi-00148. https://doi.org/10.48670/moi-00148. In Fig. 2, Scripps Argo float drift data (https://doi.org/10.6075/J0KD1Z35) were used (Zilberman et al., 2022). In Fig. 6 World Ocean Atlas 2023 (Reagan et al., 2024) was used. The atmospheric concentration of CFC12 and SF_6 after 2015 was downloaded from NOAA Global Monitoring Laboratory (https://gml.noaa.gov/hats/data.html).

Appendix A: Decadal changes in water mass properties

Eleven stations were reoccupations of previous stations (defined as stations within 20 km from our stations) at which high-precision hydrographic data had been obtained. The observed changes since the previous occupation are summarised in Table A1, and those at Station 117 and Station 83 are shown in Figs. A1 and A2, respectively.

It is known that the Standard Sea Waters used for bottle salinity measurements have batch-to-batch offsets of order 10^{-3} in Practical Salinity Scale (Uchida, 2019). These offsets were corrected by using the coefficients by Uchida (2019), but the correction was not possible for *Marion Dufresne* cruises because the batch numbers for these cruises are not known. The *Marion Dufresne* cruises used in Table A1 were conducted in 1985, 1991, and 1993. During the late 1980's to the early 1990's, cruise reports for cruises conducted under World Ocean Circulation Experiment documented use of Standard Sea Water batches from P96 to P118. The offsets for these batches scatter between -0.9×10^{-3} to 2.5×10^{-3}. It is therefore likely that salinity from *Marion Dufresne* cruises has offsets of $(-1 \sim 3) \times 10^{-3}$. In addition to the batch offset, the measurement accuracy for the *Marion Difresne* cruise was 0.003 practical salinity unit (approximately 0.003 g/kg) (Park et al., 1993). The accuracy for GO-SHIP cruises is 0.002 g/kg (Hood, 2010). The combined accuracy for the two cruises are therefore 0.004 g/kg. Adding this accuracy to the batch offset, we note that salinity differences between I07S cruise and *Marion Dufresne* cruises less than 0.007 g/kg are probably not significant. For `74DI207` on station 113, the cruise documentation records the use of batches P120 and P123 but it was not clear which was used for the station 12644 used for our comparison in Table A1. The comparison without the batch correction shows freshening of bottom water. We therefore assumed the use of P120 (batch offset -0.9×10^{-3}) rather than P123 (0.7×10^{-3}) to conservatively estimate the salinity change. The batch offsets have been applied for station 83.

In Table A1, the changes in temperature and salinity were compared on isopycnals $\gamma^n = 27.7$ and 28.27. Since previous and present data were on the same density

$$0 = \Delta\rho(\Theta, S_A, p) = \rho(-\alpha\Delta\Theta + \beta\Delta S_A) \tag{A1}$$

where α is the thermal expansion coefficient and β is the haline contraction coefficient. Once $\Delta\Theta$ is known, it is possible to calculate ΔS_A, and vice versa. Typical values of α/β are 0.21 ± 0.03 for $\Theta = 1 \pm 1°C$, $S_A = 34.9 \pm 0.1$, and $p = 3500 \pm 500$ dbar, giving approximately one to five ratio of ΔS_A to $\Delta\Theta$. We therefore use temperature for UCDW and salinity for LCDW/AABW.

UCDW became warmer by $0.09°$ to $0.17°C$ except at the stations between $40.3°S$ and $45.5°S$, where the UCDW water mass is subject to frontal movements and accompanying mesoscale mixing such that the changes are neither systematic nor robust (see also Fig. A1). As pointed out in Section 3, UCDW has a dissolved oxygen front at around $27°S$, and UCDW warming observed at stations 86 and 92 might suggest warming of the UCDW north of the front (North Indian Deep Water). Aoki et al. (2005) reported warm and salty anomalies in UCDW, which they attributed to mixing surface waters that were warmer and fresher because of climate changes. The UCDW warming found here confirms that this warming trend continued after the 1990s.

Due to the unknown possible salinity offsets of Standard Sea Water, we cannot confidently conclude freshening of LCDW and AABW except station 113. On station 113, a freshening of 0.005 g/kg after application of the offset might be significant,

Table A1. Summary of water temperature changes $\Delta\Theta$ ($^\circ$C) and salinity changes ΔS_A
(g/kg) on isopycnals from past observations to the 2019/20 occupation

station	latitude	previous	UCDW $\Delta\Theta$ $\gamma^n = 27.7$[a]	decadal $\Delta\Theta$ ($^\circ$C/ decade)	LCDW/AABW ΔS_A $\gamma^n = 28.27$[b]
78	32.2°S	Mar 1985	0.076	0.022	n/a
83	34.0°S	'87,'02,'09	n/a	n/a	n/a
86	35.0°S	Mar 1985	0.168	0.048	n/a
92	37.8°S	Mar 1985	0.092	0.026	-0.003
97	40.3°S	Mar 1985	-0.044	-0.013	n/a
103	43.0°S	Mar 1985	-0.175	-0.050	-0.002
107	45.0°S	Apr 1993	0.147	0.053	-0.002
108	45.5°S	Mar 1985	-0.207	-0.060	-0.004
113	47.7°S	Mar 1994	0.303	0.118	-0.005
115	48.0°S	Apr 1991	0.110	0.038	-0.005
117	49.0°S	Apr 1993	0.145	0.054	-0.005

a Upper Circumpolar Deep Water (UCDW) is represented at this density. Θ is Conserva-
tive Temperature.
b Lower Circumpolar Deep Water (LCDW) and Antarctic Bottom Water (AABW) are
represented at this density. S_A is Absolute Salinity.

however this station is located over the sill separating the Enderby and Crozet Basins and interpretation is difficult in the
absence of other nearby reliable data.

Bryden et al. (2003) described the water mass changes at the cross point of the GO-SHIP I05 section and the I07S section at
34°S, with a focus in the water mass changes in the thermocline (as defined by potential temperature $\theta_\sigma > 6^\circ$C) or the mode
waters in the northern Crozet Basin. Bryden et al. (2003) reported a freshening of the thermocline water mass (between potential
temperatures of 7° and 10°C) from 1987 to 2002. This cooling and freshening was also reported by Aoki et al. (2005). These
changes are attributable to surface warming in response to atmospheric warming. The freshening of the thermocline water mass
at Station 83 appears have stopped from 2002 until 2009, after which it resumed (Fig A2). This behaviour is different from that
around the salinity minimum of AAIW where the freshening from 1987 to 2002 was as large as 0.02 g/kg near the salinity
minimum at $\gamma^n = 27.4$. After 2002 the change reversed and the salinity minimum become saltier through 2009, continuing
until 2019. The salinity maximum originating from NADW at $\gamma^n = 28.05$ also shows the oscillation – saltier from 1987 to
2002 then fresher through 2009 until 2019.

These property changes have often been attributed to meridional migration of the water masses (e.g. Gille, 2002). It is
known in this region that the fronts, which are indicators of the meridional position of water masses, move southward on a
decadal timescale (Sokolov and Rintoul, 2009; Kim and Orsi, 2014). Along the I07S section, sea surface height has increased
by about 0.003 m per year north of 48°S (Fig. A3). Given the background gradient of approximately 2 m over 30° latitude,
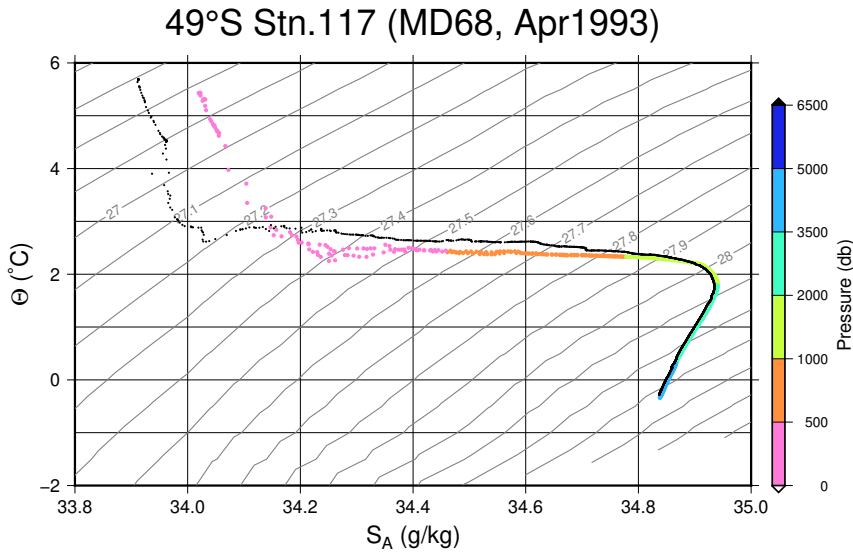
Figure A1. Water properties at Station 117 which was occupied during cruise MD68 by M/V *Marion Dufresne* in April 1993 (coloured points; the different colours indicate depth). Black points show the 2019/20 occupation results.

the fronts shifted southward roughly $0.003 \times 30/(2/30) = 1.35°$ of latitude over a period of 30 years. At the typical UCDW depth of 2000 dbar around 40°S, a close look at Fig. 4a shows that Θ does not show an obvious meridional gradient north

340 of the subtropical/subantarctic fronts at 42°S. South of the fronts, the meridional gradient of Θ is about $0.1°$C per $1°$ latitude. A southward shift of the front can therefore explain the warming observed at Stations 113, 115, and 117. Salinity at the LCDW/AABW depth of 4000 dbar shows a persistent meridional gradient of about 0.0015 g/kg per $1°$ latitude, but salinity is higher northward. A southward shift of the fronts cannot explain freshening observed at these depths. Thus a southward shift of the fronts across the I07S plausibly contributed to the UCDW warming observed south of 47°S, but other changes cannot

345 be attributed to the meridional water mass movements.

Although the seven southernmost stations south of 64°S have been occupied three times (1994, 2012, and 2019), it is difficult to identify robust trends over the two decades in this near-coastal region, which is subject to direct forcing from both the atmosphere and ice. In this appendix, we thus have argued only the changes observed in the Crozet Basin.
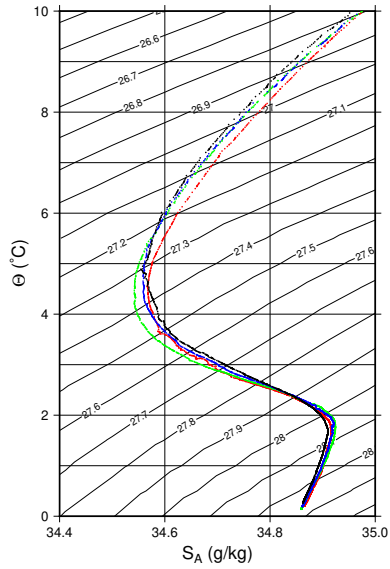
Figure A2. Water properties at Station 83, a part of the I05 section previously occupied in November 1987, March 2002, and April 2009. Data from these past occupations are shown by red, green, and blue dots, respectively, and our 2019 occupation are shown by black dots.

Appendix B: Additional figure
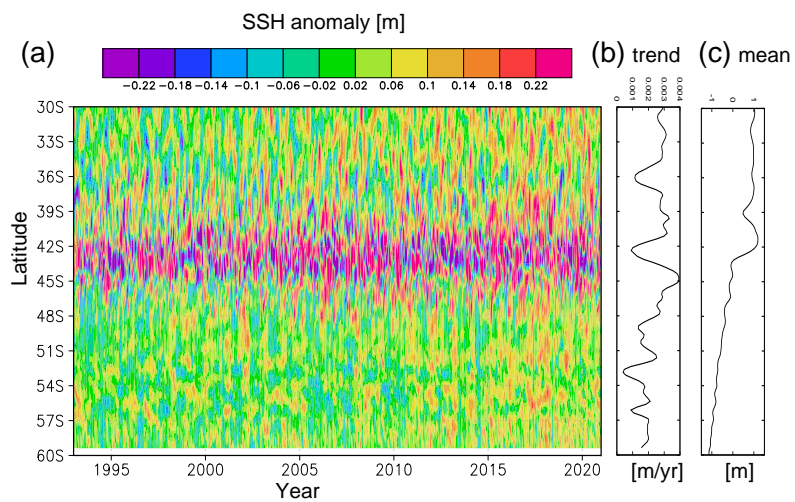
Figure A3. (a) Daily time series of the sea surface height anomalies measured by satellite altimeter along the $57.625°$S meridian. Least squares fitting at each latitude yielded profiles of (b) trend and (c) mean.
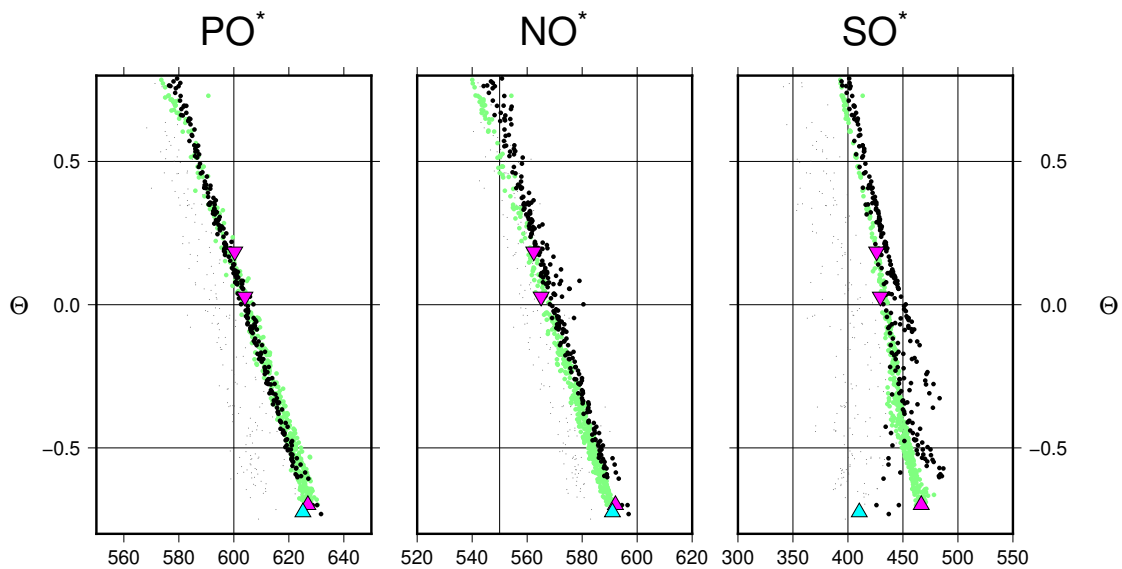
Figure B1. Pseudo-tracers $PO^* = 170[PO_4] + [O_2]$ (left), $NO^* = 10.625[NO_3] + [O_2]$ (centre), and $SO^* = 1.66[SO_4]+[O_2]$ (right) plotted against conservative temperature. The green points show deep ($\gamma^n > 28.0$) data on I06S (30°E). The black points show deep ($\gamma^n > 28.0$ and depth greater than 3000 dbar) data on I07S. The grey dots show data from the KH19 cruise. The source waters used in the mixing analysis are indicated by triangles; LCDWs by magenta inverted triangles ($PO^* =600$, $NO^*=562$, $SO^*=426$ for LCDW1; $PO^* =601$, $NO^*=565$, $SO^*=430$ for lCDW2) WSDW by the magenta triangle ($PO^* =627$, $NO^*=592$, $SO^*=467$) and CDBW by cyan triangle ($PO^* =625$, $NO^*=591$, $SO^*=410$).

350 *Author contributions.* K.K. participated in collection of the I07S data, wrote software, and wrote the original draft. S.A. conceptualised and provided methodology & interpretation. K.I.O. and M.Y.-K. collected & curated the KH data and contributed in interpretation. All authors contributed in funding acquisition, and reviewed & edited the submitted manuscript. They also contributed in the revision.

Competing interests. One of the authors is a member of the editorial board of Ocean Science.

Acknowledgements. The authors thank the officers and crew of all cruises listed in Table 1.

References

Aoki, S., Bindoff, N. L., and Church, J. A.: Interdecadal water mass changes in the Southern Ocean between 30°E and 160°E, Geophysical Research Letters, 32, https://doi.org/10.1029/2004GL022220, 2005.

Aoki, S., Katsumata, K., Hamaguchi, M., Noda, A., Kitade, Y., Shimada, K., Hirano, D., Simizu, D., Aoyama, Y., Doi, K., and Nogi, Y.: Freshening of Antarctic Bottom Water Off Cape Darnley, East Antarctica, Journal of Geophysical Research: Oceans, 125, e2020JC016 374, https://doi.org/10.1029/2020JC016374, 2020a.

Aoki, S., Yamazaki, K., Hirano, D., Katsumata, K., Shimada, K., Kitade, Y., Sasaki, H., and Murase, H.: Reversal of freshening trend of Antarctic Bottom Water in the Australian-Antarctic Basin during 2010s, Sci.Rep., 10, 14 415, https://doi.org/10.1038/s41598-020-71290-6, 2020b.

Bryden, H. L., McDonagh, E. L., and King, B. A.: Changes in Ocean Water Mass Properties: Oscillations or Trends?, Science, 300, 2086–2088, https://doi.org/10.1126/science.1083980, 2003.

Bullister, J. L. and Warner, M. J.: Atmospheric Histories (1765-2022) for CFC-11, CFC-12, CFC-113, CCl4, SF6 and N2O (NCEI Accession 0164584)., NOAA National Centers for Environmental Information, https://doi.org/10.3334/cdiac/otg.cfc_atm_hist_2015, 2017.

Bullister, J. L., Wisegarver, D. P., and Menzia, F. A.: The solubility of sulfur hexafluoride in water and seawater, Deep Sea Research Part I: Oceanographic Research Papers, 49, 175–187, 2002.

CCHDO: CCHDO Hydrographic Data Archive, UC San Diego Library Digital Collections, 10.6075/J0CCHAM8, 2023.

Fine, R. A., Smethie, W. M., Bullister, J. L., Rhein, M., Min, D.-H., Warner, M. J., Poisson, A., and Weiss, R. F.: Decadal ventilation and mixing of Indian Ocean waters, Deep Sea Research I, 55, 20–37, https://doi.org/10.1016/j.dsr.2007.10.002, 2008.

Gao, L., Zu, L., Guo, G., and Hou, S.: Recent changes and distribution of the newly-formed Cape Darnley Bottom Water, East Antarctica, Deep Sea Research Part II: Topical Studies in Oceanography, 201, 105 119, https://doi.org/10.1016/j.dsr2.2022.105119, 2022.

Gille, S. T.: Warming of the Southern Ocean Since the 1950s, Science, 295, 1275–1277, https://doi.org/10.1126/science.1065863, 2002.

Gordon, A. L. and Huber, B. A.: Thermohaline stratification below the Southern Ocean sea ice, Journal of Geophysical Research: Oceans, 89, 641–648, 1984.

Haine, T. W. N., Watson, A. J., Liddicoat, M. I., and Dickson, R. R.: The flow of Antarctic bottom water to the southwest Indian Ocean estimated using CFCs, Journal of Geophysical Research: Oceans, 103, 27 637–27 653, https://doi.org/10.1029/98JC02476, 1998.

Heywood, K. J., Sparrow, M. D., Brown, J., and Dickson, R. R.: Frontal structure and Antarctic Bottom Water flow through the Princess Elizabeth Trough, Antarctica, Deep Sea Research Part I: Oceanographic Research Papers, 46, 1181–1200, https://doi.org/10.1016/S0967-0637(98)00108-3, 1999.

Hood, M.: Introduction to the collection of expert report and guidelines, IOCCP Report No.14, https://www.go-ship.org/HydroMan.html, iCPO publication series 134, 2010.

Jackett, D. R. and McDougall, T. J.: A Neutral Density Variable for the World's Oceans, Journal of Physical Oceanography, 27, 237 – 263, https://doi.org/10.1175/1520-0485(1997)027<0237:ANDVFT>2.0.CO;2, 1997.

Johnson, G. C.: Quantifying Antarctic Bottom Water and North Atlantic Deep Water volumes, Journal of Geophysical Research: Oceans, 113, C05 027, https://doi.org/10.1029/2007JC004477, 2008.

Jullion, L., Naveira Garabato, A. C., Bacon, S., Meredith, M. P., Brown, P. J., Torres-Valdés, S., Speer, K. G., Holland, P. R., Dong, J., Bakker, D., Hoppema, M., Loose, B., Venables, H. J., Jenkins, W. J., Messias, M.-J., and Fahrbach, E.: The contribution of the

Weddell Gyre to the lower limb of the Global Overturning Circulation, Journal of Geophysical Research: Oceans, 119, 3357–3377, https://doi.org/10.1002/2013JC009725, 2014.

Katsumata, K.: Eddies Observed by Argo Floats. Part II: Form Stress and Streamline Length in the Southern Ocean, Journal of Physical Oceanography, 47, 2237 – 2250, https://doi.org/10.1175/JPO-D-17-0072.1, 2017.

395 Katsumata, K. and Yamazaki, K.: Diapycnal and isopycnal mixing along the continental rise in the Australian–Antarctic Basin, Progress in Oceanography, 211, 102 979, https://doi.org/10.1016/j.pocean.2023.102979, 2023.

Katsumata, K., Talley, L. D., Capuano, T. A., and Whalen, C. B.: Spatial and Temporal Variability of Diapycnal Mixing in the Indian Ocean, Journal of Geophysical Research: Oceans, 126, e2021JC017 257, https://doi.org/10.1029/2021JC017257, 2021.

Kim, Y. S. and Orsi, A. H.: On the Variability of Antarctic Circumpolar Current Fronts Inferred from 1992–2011 Altimetry, Journal of
400 Physical Oceanography, 44, 3054 – 3071, https://doi.org/10.1175/JPO-D-13-0217.1, 2014.

Kusahara, K., Williams, G. D., Tamura, T., Massom, R., and Hasumi, H.: Dense shelf water spreading from Antarctic coastal polynyas to the deep Southern Ocean: A regional circumpolar model study, Journal of Geophysical Research: Oceans, 122, 6238–6253, https://doi.org/10.1002/2017JC012911, 2017.

Ledwell, J. R.: The Brazil Basin Tracer Release Experiment: Observations, Journal of Physical Oceanography, 54, 1105 – 1120,
405 https://doi.org/10.1175/JPO-D-22-0249.1, 2024.

Madsen, K., Nielsen, H. B., and Tingless, O.: Methods for non-linear least squares problems, Informatics and Mathematical Modelling, Technical University of Denmark, http://www.imm.dtu.dk/pubdb/views/edoc_download.php/3215/pdf/imm3215.pdf, 2nd Edition, downloaded on 7th February 2024, 2004.

Mantyla, A. W. and Reid, J. L.: Abyssal characteristics of the World Ocean waters, Deep Sea Research Part A. Oceanographic Research
410 Papers, 30, 805–833, 1983.

McDougall, T. J.: The relative roles of diapycnal and isopycnal mixing on subsurface water mass conversion, Journal of Physical Oceanography, 14, 1577–1589, 1984.

Meijers, A. J. S., Klocker, A., Bindoff, N. L., Williams, G. D., and Marsland, S. J.: The circulation and water masses of the Antarctic shelf and continental slope between 30 and 80°E, Deep Sea Research Part II: Topical Studies in Oceanography, 57, 723–737,
415 https://doi.org/10.1016/j.dsr2.2009.04.019, 2010.

Menezes, V. V., Macdonald, A. M., and Schatzman, C.: Accelerated freshening of Antarctic Bottom Water over the last decade in the Southern Indian Ocean, Science Advances, 3, e1601 426, https://doi.org/10.1126/sciadv.1601426, 2017.

Meredith, M. P., Locarnini, R. A., Van Scoy, K. A., Watson, A. J., Heywood, K. J., and King, B. A.: On the sources of Weddell Gyre Antarctic Bottom Water, Journal of Geophysical Research: Oceans, 105, 1093–1104, https://doi.org/10.1029/1999JC900263, 2000.

420 Ohashi, Y., Yamamoto-Kawai, M., Kusahara, K., Sasaki, K., and Ohshima, K. I.: Age distribution of Antarctic Bottom Water off Cape Darnley, East Antarctica, estimated using chlorofluorocarbon and sulfur hexafluoride, Scientific Reports, 12, 8462, https://doi.org/10.1038/s41598-022-12109-4, 2022.

Ohshima, K., Fukamachi, Y., Williams, G. D., Nihashi, S., Roquet, F., Kitade, Y., Tamura, T., Hirano, D., Herraiz-Borreguero, L., Field, I., Hindell, M., Aoki, S., and Wakatsuchi, M.: Antarctic Bottom Water production by intense sea-ice formation in the Cape Darnley polynya,
425 Nature Geoscience, 6, 235–240, 2013.

Orsi, A. H., Whitworth III, T., and Nowlin Jr, W. D.: On the meridional extent and fronts of the Antarctic Circumpolar Current, Deep Sea Research Part I: Oceanographic Research Papers, 42, 641–673, 1995.

Orsi, A. H., Johnson, G. C., and Bullister, J. L.: Circulation, mixing, and production of Antarctic Bottom Water, Progress in Oceanography, 43, 55–109, https://doi.org/10.1016/S0079-6611(99)00004-X, 1999.

430 Park, Y.-H. and Gambéroni, L.: Cross-frontal exchange of Antarctic Intermediate Water and Antarctic Bottom Water in the Crozet Basin, Deep Sea Research Part II: Topical Studies in Oceanography, 44, 963–986, https://doi.org/10.1016/S0967-0645(97)00004-0, 1997.

Park, Y.-H., Gambéroni, L., and Charriaud, E.: Frontal structure and transport of the Antarctic Circumpolar Current in the south Indian Ocean sector, 40–80°E, Marine Chemistry, 35, 45–62, https://doi.org/10.1016/S0304-4203(09)90007-X, 1991.

Park, Y.-H., Gambéroni, L., and Charriaud, E.: Frontal structure, water masses, and circulation in the Crozet Basin, Journal of Geophysical
435 Research: Oceans, 98, 12 361–12 385, https://doi.org/10.1029/93JC00938, 1993.

Park, Y.-H., Charriaud, E., and Fieux, M.: Thermohaline structure of the Antarctic Surface Water/Winter Water in the Indian sector of the Southern Ocean, Journal of Marine Systems, 17, 5–23, https://doi.org/10.1016/S0924-7963(98)00026-8, 1998.

Phillips, H. E. and Rintoul, S. R.: Eddy Variability and Energetics from Direct Current Measurements in the Antarctic Circumpolar Current South of Australia, Journal of Physical Oceanography, 30, 3050 – 3076, https://doi.org/10.1175/1520-
440 0485(2000)030<3050:EVAEFD>2.0.CO;2, 2000.

Polzin, K. L., Naveira Garabato, A. C., Huussen, T. N., Sloyan, B. M., and Waterman, S.: Finescale parameterizations of turbulent dissipation, Journal of Geophysical Research: Oceans, 119, 1383–1419, https://doi.org/10.1002/2013JC008979, 2014.

Reagan, J. M., Boyer, T. P., García, H. E., Locarnini, R. A., Baranova, O. K., Bouchard, C., Cross, S. L., Mishonov, A. V., Paver, C. R., Seidov, D., Wang, Z., and Dukhovskoy, D.: World Ocean Atlas 2023, NOAA National Centers for Environmental Information., accession
445 0270533, 2024.

Reiniger, R. F. and Ross, C. K.: A method of interpolation with application to oceanographic data, Deep Sea Research and Oceanographic Abstracts, 15, 185–193, https://doi.org/10.1016/0011-7471(68)90040-5, 1968.

Ryan, S., Schröder, M., Huhn, O., and Timmermann, R.: On the warm inflow at the eastern boundary of the Weddell Gyre, Deep Sea Research Part I: Oceanographic Research Papers, 107, 70–81, https://doi.org/10.1016/j.dsr.2015.11.002, 2016.

450 Sasaki, Y., Yasuda, I., Katsumata, K., Kouketsu, S., and Uchida, H.: Turbulence across the Antarctic Circumpolar Current in the Indian Southern Ocean: Micro-Temperature Measurements and Finescale Parameterizations, Journal of Geophysical Research: Oceans, 129, e2023JC019 847, https://doi.org/10.1029/2023JC019847, 2024.

Schlosser, P., Bullister, J. L., and Bayer, R.: Studies of deep water formation and circulation in the Weddell Sea using natural and anthropogenic tracers, Marine Chemistry, 35, 97–122, 1991.

455 Sokolov, S. and Rintoul, S. R.: Circumpolar structure and distribution of the Antarctic Circumpolar Current fronts: 2. Variability and relationship to sea surface height, Journal of Geophysical Research: Oceans, 114, https://doi.org/10.1029/2008JC005248, 2009.

Tulloch, R., Ferrari, R., Jahn, O., Klocker, A., LaCasce, J., Ledwell, J. R., Marshall, J., Messias, M.-J., Speer, K., and Watson, A.: Direct Estimate of Lateral Eddy Diffusivity Upstream of Drake Passage, Journal of Physical Oceanography, 44, 2593 – 2616, https://doi.org/10.1175/JPO-D-13-0120.1, 2014.

460 Uchida, H.: The latest batch-to-batch correction table for IAPSO Standard Seawater, https://doi.org/10.17596/0001983, 2019.

Uchida, H., Shimada, K., and Kawano, T.: A Method for Data Processing to Obtain High-Quality XCTD Data, Journal of Atmospheric and Oceanic Technology, 28, 816 – 826, https://doi.org/10.1175/2011JTECHO795.1, 2011.

Uchida, H., Murata, A., Katsumata, K., Arulananthan, K., and Doi, T.: WHP I08N revisit/I07S in 2019/2020 data book, https://doi.org/10.17596/0002118, available from the same location as the hydrographic data., 2021.

465 Warner, M. J. and Weiss, R. F.: Solubilities of chlorofluorocarbons 11 and 12 in water and seawater, Deep Sea Research Part A., 32, 1485–1497, 1985.

Warren, B. A.: Bottom water transport through the Southwest Indian Ridge, Deep Sea Research, 25, 315–321, https://doi.org/10.1016/0146-6291(78)90596-9, 1978.

Williams, G. D., Nicol, S., Aoki, S., Meijers, A. J. S., Bindoff, N. L., Iijima, Y., Marsland, S. J., and Klocker, A.: Surface oceanogra-
470   phy of BROKE-West, along the Antarctic margin of the south-west Indian Ocean (30–80◦E), Deep Sea Research Part II, 57, 738–757, https://doi.org/10.1016/j.dsr2.2009.04.020, 2010.

Zilberman, N. V., Scanderbeg, M. C., Gray, A. R., and Oke, P. R.: Scripps Argo trajectory-based velocity product 2001-01 to 2020-12, UC San Diego Library Digital Collections, https://doi.org/10.6075/J0KD1Z35, in Scripps Argo Trajectory-Based Velocity Product, 2022.